PHOTONICS Research

High-speed adaptive photoacoustic microscopy

LINYANG LI,[1,†] WEI QIN,[1,†] TINGTING LI,[1] JUNNING ZHANG,[1] BAOCHEN LI,[1] AND LEI XI[1,2,3,*] (iD)

[1]*Department of Biomedical Engineering, Southern University of Science and Technology, Shenzhen 518055, China*
[2]*Guangdong Provincial Key Laboratory of Advanced Biomaterials, Southern University of Science and Technology, Shenzhen 518055, China*
[3]*Shenzhen Bay Laboratory, Shenzhen 518132, China*
[†]*These authors contributed equally to this work.*
Corresponding author: xilei@sustech.edu.cn

Optical-resolution photoacoustic microscopy (OR-PAM) is capable of observing the distribution of optical absorbers inside bio-tissues with a high spatial resolution of micrometers. Unfortunately, due to the employment of a tight optical focus, it suffers from a limited depth of field (DOF), making it challenging to achieve high-resolution imaging of targets with arbitrary surfaces. Here, we propose a high spatiotemporal adaptive photoacoustic focusing mechanism through integrating a high-speed optical focuser, a time-of-flight contour deriving algorithm, and the rotary-scanning photoacoustic microscopy. The developed system, named high-speed adaptive photoacoustic microscopy (HA-PAM), features an ultrashort focus-shifting time of 5 ms and an enlarged DOF of up to 5 mm. With the assistance of the proposed mechanism, we can achieve a homogeneous lateral resolution of 6 μm over a 10 mm circular imaging domain within 5 s. We demonstrate the advantages of HA-PAM through imaging phantoms with curved surfaces, subcutaneous tumor-bearing mice, resected rabbit kidneys, and pulsating mouse brains. The imaging results suggest that this approach provides a high and consistent spatial resolution for imaging bio-tissues with arbitrary surfaces without sacrificing the imaging speed, and has the potential to extend the fundamental and clinical applications of OR-PAM. © 2023 Chinese Laser Press

https://doi.org/10.1364/PRJ.499598

1. INTRODUCTION

Hemodynamic changes, cerebral revascularization, and neuro-hemodynamic coupling are critical factors in the reflection of brain functions. In recent decades, various optical imaging methodologies such as fluorescence imaging, optical intrinsic signal imaging, and laser speckle contrast imaging, have been used to study rapidly changing cerebral hemodynamics [1–3]. Among these optical imaging techniques, optical resolution photoacoustic microscopy (OR-PAM), as an emerging optical imaging modality, detects absorption-induced acoustic signals to directly visualize the distribution of intrinsic or extrinsic optical absorbers [4–6], and has been widely applied in functional brain imaging [7–9]. However, OR-PAM usually suffers from a restricted depth of field (DOF) due to the use of a tight optical focus to achieve diffraction-limited resolution [10–12]. This narrow DOF causes the degradation of lateral resolution at the off-focus planes. For applications of imaging irregular surfaces, especially time-sensitive ones such as various studies of whole cortex functions, there is a desire to capture images with a large DOF, a high spatiotemporal resolution, and a sufficient field of view (FOV). In addition, in *in vivo* imaging of large rodents and primates, motions due to heart beating, breathing,

and brain pulsation may induce unpredictable out-of-focus deterioration of image quality.

To address the need for high spatiotemporal imaging with a large FOV and an extended DOF in OR-PAM, various approaches have been explored. Modulations of light including non-diffracting beams [13–16] and structured illumination [17–19] have been combined with OR-PAM to extend the DOF and attenuate out-of-focus impact on the image quality. However, these methods usually face one or more limitations such as severe sidelobes, low efficiency, slow imaging speed, and complicated post-processing procedures. In addition, the extended DOF is not sufficient to cover curved tissue surfaces of medium to large animals. Recently, a dynamic remote focusing approach has achieved a large DOF with the requirement of pre-scanning [20,21], multifocus imaging [22–27], or contour scanning [28,29] using three-dimensional motors, which leads to extra imaging time, inconsistent spatial resolution, or complicated mechanical structure.

To fill this gap, we apply a high-speed adaptive focusing photoacoustic mechanism in the rotary-scanning-based OR-PAM [8,30,31], termed as HA-PAM. We employ the time-of-flight information carried by photoacoustic signals and a high-speed focuser to extract the surface contour and enable

real-time adjustment of the focal plane, respectively. The HA-PAM exhibits a high lateral resolution of 6 μm, an ultra-short focus-shifting time of 5 ms, a temporal resolution of 0.2 Hz over a circular FOV with a diameter of 10 mm, and an enlarged DOF of 5 mm. We demonstrate the advantages of HA-PAM in the imaging of biological tissues with large curvatures including subcutaneous tumors and rabbit kidneys. In addition, we apply HA-PAM to study the fast cerebral hemodynamics *in vivo*, where there exist severe out-of-focus issues caused by the curved brain surface and physiological activities including breathing and cortical pulsations. These results demonstrate the superior imaging performance of HA-PAM in the studies of uneven tissues and brain functions.

2. RESULTS

A. System Design and Principle of HA-PAM

Figure 1(a) shows the schematic of the experimental setup, where HA-PAM utilizes a nanosecond-pulsed laser (GLPN-16-1-10-M, IPG Photonics) to emit 532 nm excitation pulses, a pair of achromatic doublets, and a high-energy pinhole to spatially filter and expand the laser beam to obtain a Gaussian beam with a spot diameter of 6 mm. The collimated laser beam is focused onto the tissue surface via an objective (AC127-050-A, Thorlabs) that is mounted on a high-speed focuser (HSF, BLINK, Thorlabs) to achieve fast adjustment of the laser focus. We employ a two-dimensional galvanometer scanner (GVS002, Thorlabs) to achieve laser beam scanning. The optically excited ultrasonic waves are reflected by a glass (G) and detected by a customized cylindrically focused ultrasound transducer (Olympus IMS) with a center frequency of 15 MHz. The photoacoustic (PA) signals are amplified by a 60 dB amplifier (PAOMTek), filtered by a 5–30 MHz bandpass filter, and acquired by a high-speed data acquisition board (ATS9350, Alazar Technologies) at a sampling rate of 500 MS/s. We use a multifunction I/O device (PCI-6733, National Instruments) to achieve synergistic coordination of laser scanning, transducer rotation, and translation of the high-speed focuser.

According to the principle of PAM, each PA signal excited by a single laser pulse, termed as A-line [Fig. 1(a), bottom left], involves the depth-resolved information. Stacking a sequence of A-lines generated by one-dimensional scanning of the laser spot forms a cross-sectional slice named B-scan. Apart from conventional raster scanning, in rotary scanning, B-scans are collected in sequence as the ultrasound transducer rotates along the tangential direction [Fig. 1(b)]. Compared to polygon scanning requiring correction of depth information [12], we can easily calculate the displacement (Δz) between the imaging plane and the focal plane with the derived time intervals (Δt) from A-lines and given acoustic velocity in the tissues. Then, we drive the objective lens via the HSF to ensure that the imaging plane is always overlapped with the focal plane during the imaging. Considering the continuity of the tissue surface, we use the prior B-scan to predict the surface profile and control the trajectory of the laser spot via the HSF during the next B-scan scanning [Fig. 1(c)]. For example, in the kth B-scan, we identify the position of the peak value in each A-line and carry out curve fitting of the peak-value points to derive the contour
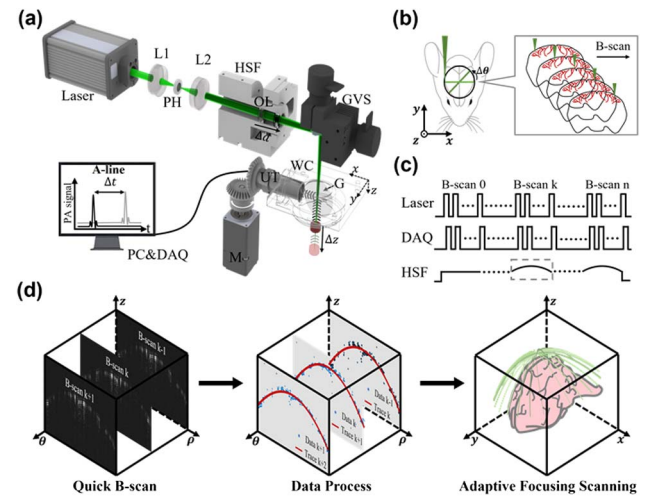

Fig. 1. System schematic and principle of HA-PAM. (a) Experimental setup of the HA-PAM system. L1, L2, achromatic doublet; PH, pinhole; HSF, high-speed focuser; OL, objective lens; GVS, galvanometer scanner; WC, water cube; G, glass; UT, ultrasound transducer; DAQ, data acquisition. (b) HA-PAM scanning scheme. Volumetric imaging is achieved by two-dimensional rotary scanning. (c) Synchronization sequences of laser excitation, data acquisition, and high-speed focuser. (d) The principle of adaptive focusing.

profile of the imaging plane as well as the coordinate. Then, we extract the trajectory and drive the HSF following the trajectory in the $(k + 1)^{th}$ B-scan to compensate for the out-of-focus deterioration induced by motions and surface curvature to achieve adaptive focusing scanning [Fig. 1(d)]. The same procedure is repeated until the completion of the image acquisition. Therefore, compared to existing methods, HA-PAM can extract the contour in the entire imaging domain without pre-scanning/imaging the objects.

B. High Spatiotemporal Imaging with a Large FOV

HA-PAM employs a post-objective scanning configuration where the galvanometer scanner is positioned after the objective and the size of the optical focus in the center is much smaller than that in the edge over the entire FOV [Fig. 2(a) and Fig. 5 in Appendix B]. We optimize the axial location of the objective for each excitation position and generate a trajectory of the objective during the scanning to achieve a flat FOV with a consistent lateral resolution [Fig. 6(a) in Appendix C]. The theoretical resolution in each position is determined using the optical transfer function [Fig. 6(b) in Appendix C]. Figure 2(b) shows the difference of the theoretical resolution in different regions across the FOV before and after calibrating the focal plane as highlighted by the gray box in Fig. 2(a). By imaging a sharp edge of a blade in two different regions using HA-PAM, Fig. 2(c) displays the fitted edge spread function perpendicular to the edge and the calculated line spread function (LSF), where the measured full width at half-maximum of the LSF indicates a consistent lateral resolution of ~6 μm over the entire FOV. The maximum amplitude projection (MAP) of a reticle using HA-PAM shows that the distortion and resolution deterioration have been fully eliminated within the FOV [Fig. 2(a)].
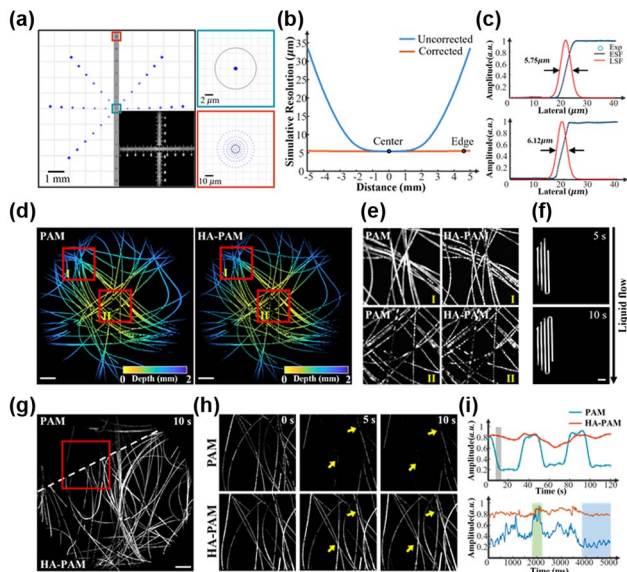
Fig. 2. Experimental demonstration of a high spatiotemporal resolution, large FOV, and an ultrahigh sensitivity of HA-PAM. (a) The imaging FOV and individual spot sizes within the FOV. (b) Simulation of resolution distribution using Zemax. (c) Lateral resolutions measured by imaging a sharp edge. The lateral resolution of the calibrated focal plane in the center (top) and edge (bottom) areas. Exp, experimental data; ESF, edge spread function; LSF, line spread function. (d) Depth-resolved imaging of the phantom with curved surfaces from conventional PAM and HA-PAM. Scale bars, 1 mm. (e) Close-up MAP images of the red box region in (d). The region II of the image corresponds to the areas surrounding the optical focal plane, which exhibits a higher SNR and a better resolution compared to the out-of-focus areas (region I). (f) Black ink flows in a microfluidic channel. Scale bars, 1 mm. (g) The image of the carbon fibers obtained using conventional PAM and HA-PAM with simulated brain pulsation. (h) Close-up images of the area indicated by the red box in (g) show the difference between conventional PAM and HA-PAM. Massive missing features of the conventional PAM image are marked by the yellow arrows. (i) Variation curves of the average signal amplitude of a selected ROI for different time spots using conventional PAM and HA-PAM, respectively. Scale bars, 1 mm.

To reveal the superiority of the extended DOF ∼30° using adaptive focusing, we image a tilted pencil lead inserted into an agarose phantom with an angle of ∼30° [Fig. 7(a) in Appendix D], where the vertical distance between two tips is about 5 mm. The conventional PAM image shows limited features and decreased SNR when scanning the out-of-focus area of the pencil lead due to the limited DOF [Fig. 7(b) in Appendix D]. In contrast, the HA-PAM image shows a complete geometry of the pencil lead with a homogeneous resolution and SNR over the entire imaging domain, indicating that the HA-PAM has an extended DOF of 5 mm. Figure 2(d) shows the depth-encoded MAP images of carbon fibers embedded inside a tissue-mimicking phantom with a curved surface using conventional PAM and HA-PAM, respectively. By applying adaptive focusing, we can clearly observe significantly improved resolution in the off-center area [Fig. 2(e)]. We assess the high-speed imaging capability of HA-PAM by observing the liquid flow in a microfluidic chip [Fig. 2(f); Visualization 1 shows the black ink flowing process].

To confirm the feasibility of HA-PAM for overcoming the out-of-focus problem due to physiological activities in *in vivo* imaging, we design a multilayer chip with an inside cavity using polydimethylsiloxane (PDMS), including a carbon fiber layer, a sealing layer, and a basal layer. To simulate physiological phenomena such as brain pulsation and respiration, the carbon fiber layer can achieve anisotropic expansion and contraction by using a micro-syringe pump (TYD02-01, Lead Fluid) to inject or extract air into the cavity (Fig. 8 in Appendix E). The images using conventional PAM and HA-PAM of the carbon fiber layer [Fig. 2(g)] show that the areas near the optical focal plane have a better SNR and resolution than those in the out-of-focus areas. Visualization 2 shows the images using conventional PAM and HA-PAM during the random shrinkage and expansion of the carbon fibers layer, respectively. During the entire imaging process, the close-up images using conventional PAM [top panel in Fig. 2(h)] have lost massive features as highlighted by the yellow arrows, which are caused by the anisotropic expansion and contraction of the carbon fibers. In contrast, the HA-PAM images [bottom panel in Fig. 2(h)] show the consistent well-resolved features during the movement of the carbon fibers over the entire imaging domain. In quantitative comparison, the average signal amplitude of the PA signals in the conventional PAM image [Fig. 2(i)] is more volatile than that of HA-PAM. This further demonstrates that HA-PAM with adaptive adjustment of the optical focal plane to follow the movement of the target enables more consistent imaging under dynamic scenarios.

C. Imaging of Biological Tissues with Large Curved Surfaces

Obtaining large-FOV, high-resolution images of biological tissues with irregular tissue surfaces is always challenging. We carried out conventional PAM [Figs. 9(a)–9(c) in Appendix F] and HA-PAM [Figs. 3(a), 3(d), and 3(g)] imaging of subcutaneous mouse tumors, resected rabbit kidneys, and mice brains.

Compared with conventional PAM, HA-PAM captures more vessel features of tumors, as highlighted in Fig. 3(b). Figure 3(c) [the close-up image in Fig. 3(b)] shows that HA-PAM is able to distinguish denser vessel networks, whereas the corresponding area in the conventional PAM image is blurred. The intensity profiles of the selected vessel indicated by the lines in Fig. 3(c) exhibit the superior spatial resolving capability and SNR of HA-PAM compared to conventional PAM. In addition to tumors, we further carried out imaging of resected rabbit kidneys that have large-curved surfaces. We processed the samples with optical transparency and contrasted them with ink solution in renal veins [32]. Figures 3(e) and 3(f) present the acquired MAP images and selected regions of interest (ROIs) using both conventional PAM and HA-PAM, respectively. As we expected, the detailed vascular structures distributed in the off-center areas of the kidney cannot be well resolved by conventional PAM. Figure 3(f) shows the close-up area indicated by the blue box in Fig. 3(e), where the homogeneous high lateral resolution enables HA-PAM to provide more details of peripheral blood vessels in the venous system of the kidney over the entire FOV. The close-up image of the area indicated by the white box in Fig. 3(g) shows the difference between HA-PAM and conventional PAM [Fig. 3(h)].
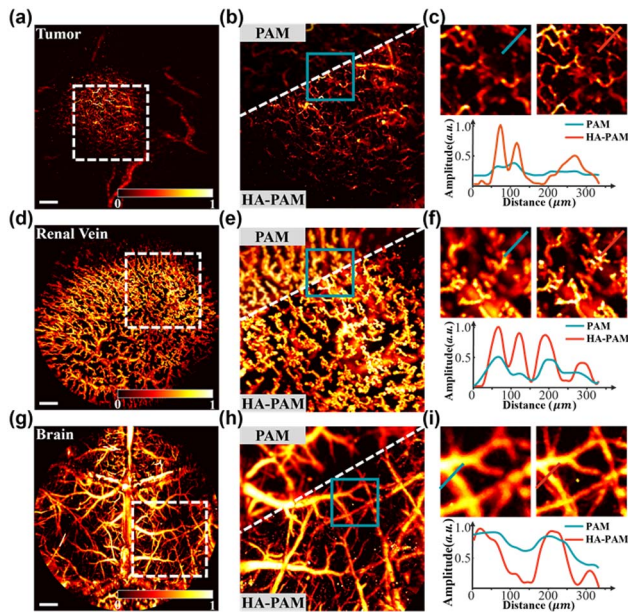
Fig. 3. HA-PAM and conventional PAM of mice subcutaneous tumors, rabbit kidneys, and mouse brains. (a), (d), and (g) Images of a subcutaneous mice tumor (a), the venous system of a resected rabbit kidney (d), and a mouse brain (g) using HA-PAM. Scale bars, 1 mm. (b) Close-up images of the area indicated by the white dashed box in (a) show the differences between HA-PAM and conventional PAM. (c) Close-up images of the representative area using conventional PAM (left) and HA-PAM (right). (e) Close-up images of the area indicated by the white dashed box in (d) show the blurred microvasculature due to the out-of-focus issue. (f) Close-up images of the representative area show that HA-PAM (right) had a better resolution than conventional PAM (left). (h) Close-up images of the area indicated by the white dashed box in (g) using HA-PAM and conventional PAM. (i) Comparison of close-up conventional PAM image (left) with close-up HA-PAM image (right). The cross-sectional profiles of the vessels marked by the lines in (c), (f), and (i) show the well-maintained resolution in the corresponding areas using HA-PAM.

The conventional PAM image of a mouse brain shows blurred vessels in the close-up image as well as missing features, which are caused by the limited DOF and the large curvature of the brain surface [Fig. 3(i)]. In contrast, the HA-PAM image of the brain shows well-resolved brain features that are not identifiable in the conventional PAM image. HA-PAM does not require additional data processing or time-consuming pre-scanning to acquire high-quality structural information of the vascular network on the curved surface of large biological tissues, which is crucial for time-sensitive imaging and subsequent analysis.

D. Fast Imaging of Pulsating Cerebral Cortex Using HA-PAM

With the capability of observing oxyhemoglobin and deoxyhemoglobin in a label-free manner, PAM has been widely used to investigate both the brain vasculature and functions. However, the large curvature of the cerebral cortex and brain pulsation propose the hassle to achieve high spatiotemporal observation of the entire cerebral cortex due to the severe out-of-focus deterioration of image quality. To demonstrate that HA-PAM is capable of addressing such issues, we carried out mouse

brain imaging with simulated brain pulsation via a motorized translation.

We used a one-dimensional motor to drive the mice to move freely in the direction perpendicular to the imaging plane (Fig. 10 in Appendix G). The image of the mouse brain [Fig. 4(a)] shows that the areas near the optical focal plane have a finer vascular structure than that in the out-of-focus areas. Visualization 3 shows the imaging results using both conventional PAM and HA-PAM during the entire motion process with motorized translation. The close-up image of the conventional PAM [Fig. 4(b), left] shows severe missing microvasculature (indicated by green arrows) due to the simulated movement in contrast to the image acquired by HA-PAM [Fig. 4(b), right]. The cross-sectional profiles of two representative brain regions through both imaging approaches show more blurred vessels in the conventional PAM image compared to the counterparts captured by HA-PAM [Fig. 4(c)]. Figure 4(d) indicates that conventional PAM only recovers detailed features near the optical focal plane, while HA-PAM achieves high-resolution imaging consistently over the entire FOV throughout the imaging process. It is worth mentioning that the vessels disappearance in Fig. 4(d) may be due to the physiological activity of the mouse itself. Figures 4(e) and 4(f) plot the variations of branches and averaged PA amplitude derived from the conventional PAM and HA-PAM images, respectively, revealing that HA-PAM has a higher SNR and more consistent resolution during the whole imaging process. We further identified and segmented the vascular network [33] [Fig. 4(g)], derived the variation of concentration of hemoglobin total (C_{HbT}) in the area marked by blue circles in Fig. 4(g), investigated the relative size change of two selected vessels marked by I and II in Fig. 4(g), and plotted the curves in Figs. 4(h) and 4(i). The results suggest that HA-PAM is not sensitive to the movement of the brain and keeps a smaller fluctuation of C_{HbT} and vessel size compared with conventional PAM, which can eliminate serious erroneous effects on the subsequent hemodynamic studies [1,8,9].

3. DISCUSSION AND CONCLUSION

In this study, we proposed HA-PAM that has simultaneously achieved a high spatial resolution, a high imaging speed, a large FOV, and an ultra-large DOF. By using a combination of adaptive focus and rotary scanning scheme, HA-PAM can achieve 200 Hz adaptive focus scanning with an imaging frame rate of 0.2 Hz, a varied lateral resolution of 5.8 to 6.2 μm, and an ultra-large DOF of 5 mm over an FOV of 10 mm. According to the advantages, HA-PAM can image large irregular biological tissues with a uniformly high spatial resolution and eliminate the potential out-of-focus impact by physiological activities such as breathing, uncontrollable movement, and brain pulsation. In our current setup, the performance of the HSF is the primary limitation that constrains the maximum imaging and focus speeds. The use of a faster motor could further enhance the imaging performance of the entire system. In addition, the load capacity of the HSF is limited to 50 g and not compatible with regular objectives, which might confine the applicable scenarios. It is worth mentioning that the ultrasound transducer also has a limited DOF, which affects the detection sensitivity of photoacoustic signals at different
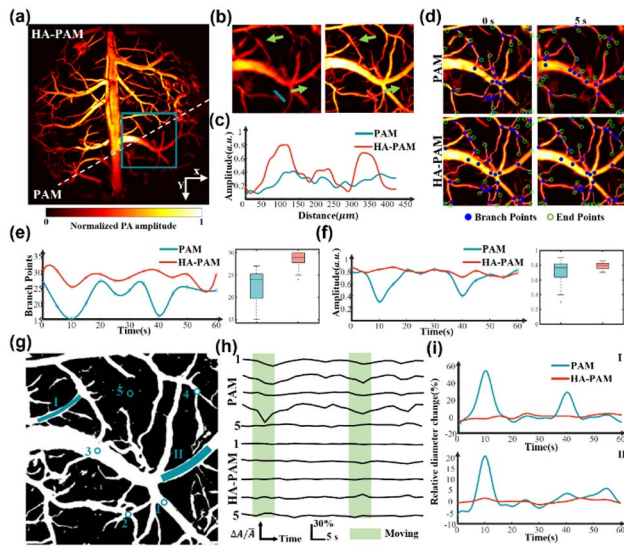
Fig. 4. Conventional PAM and HA-PAM for *in vivo* imaging with simulated breathing and brain pulsation. (a) The images of a mouce brain obtained using conventional PAM and HA-PAM. Scale bar, 1 mm. (b) Close-up images of the area indicated by the blue box in (a). (c) Cross-sectional profiles of the representative mice brain marked by the lines in (b). (d) The derived branch and end points of the vascular network. (e), (f) Variation curves of the branch and averaged amplitude in the close-up region at different time spots. (g) The segmentation mask for the vascular network. (h) Temporal variation of the C_{HbT} ($\Delta A/\bar{A}$, A is the PA signal amplitude) in five selected areas marked by blue circles in (g). The green areas indicate the simulated movement by the motor. (i) Temporal variation of the vessel diameter ($\Delta d/\bar{d}$, d is the vessel diameter) of the marked I and II in (g).

depths. Therefore, considering the image quality, the maximum extended DOF of HA-PAM is set to 5 mm.

The exceptional performance of HA-PAM was first demonstrated through imaging subcutaneous tumors and resected rabbit kidneys. The results suggest that HA-PAM provides remarkable adaptive focusing to effectively mitigate the out-of-focus issue that is caused by the uneven surface of the object. We further carried out HA-PAM imaging of the mouse cerebral cortex with simulated pulsation, where HA-PAM can quickly adjust the focal plane according to the observed regular motions. The capability of HA-PAM to maintain high image quality in different out-of-focus scenarios has significant implications for the advancement of biomedical research and clinical applications.

HA-PAM utilizes a post-objective laser scanning method coupled with an additional high-frequency Z-axis scanning. Unlike conventional PAM systems, this method achieves compact photoacoustic microscopic imaging of 3D contoured samples with a high resolution and a large FOV. Table 1 in Appendix H compares our HA-PAM approach with previously developed methods for extending DOF values in PAM. Compared to PAM using non-diffracting beams, such as Bessel beam [14,16] or needle beam [19], HA-PAM provides a larger extended DOF. Compared with the dynamic remote focusing approach [24,25], HA-PAM provides a

consistent, near-diffraction-limit resolution. Compared to previous contour-scanning PAM methods [21,28,29] that use a three-dimensional motor, adaptive focus algorithms eliminate the need for pre-scanning or multifocal plane fusion, enabling HA-PAM to achieve high imaging speed.

Due to the universality of this adaptive focusing approach, using multispectral illumination, HA-PAM can provide more functional information, including absolute concentrations of HbO and Hb, cerebral metabolic rate of oxygen, oxygen saturation in the blood vessels, and absolute velocity of blood flow [9,34,35]. Moreover, rotary-scanning-based HA-PAM is flexibly compatible with other optical imaging modalities such as optical coherent tomography, laser scanning confocal microscopy, and laser speckle imaging.

In summary, we have developed a high spatiotemporal wide-field PAM technology with adaptive focusing to significantly extend the DOF and overcome the impact of physiological activities, which thus enables accurate imaging and makes it accessible to different scenarios.

APPENDIX A: EXPERIMENTAL SECTION

Phantom Experiments: In the evaluation experiments, the blade was inserted on the surface of a tissue-mimicking agarose phantom. Lateral resolution was measured by imaging a sharp edge of the blade, quantified using edge spread functions and derived line spread functions. The carbon fiber phantom was made by randomly distributing carbon fibers with a diameter of ~6 μm embedded in an agarose block. Another ultrathick tissue-mimicking phantom, which utilized agar gel (thickness 5 mm) inserted with a pencil lead (diameter 0.5 mm), was applied to examine the extended DOF of the system.

Preparation of Chips and Experiment: The microfluidic chip was fabricated with PDMS and had one inlet and one outlet. The width and height of the channel were both 250 μm. The thickness of the sealing PDMS membrane on the top of the channel was ~100 μm to minimize the attenuation of the PA signal. We used a micro-syringe pump (TYD02-01, Lead Fluid) to inject the black ink into the channel at a fixed flow rate of 0.1 nL/s. In phantom experiments with simulated brain pulsation, we designed a multilayer chip with an inner cavity. Figure 8(b) in Appendix E shows the fabrication of the chip chamber. The PDMS pre-polymer (SYLGARD 184 silicone elastomer Dow Corning) and curing agent (SYLGARD184 - silicone elastomer curing agent, Dow Corning) were weighted and thoroughly mixed in a Petri dish at a ratio of 10:1. The Petri dish with the mixture was placed into a vacuum container to remove the air bubbles. Then, most of the mixture was poured into a customized model. Part of the mixture was poured onto the center of an acrylic plant and spun at a speed of 1000 r/min for 30 seconds to form a smooth 100 μm thickness PDMS film. Then, carbon fibers were distributed on the surface of the PDMS film. After vacuum degassing and solidification, we obtained the basal layer, sealing layer, and carbon fiber layer. Finally, these layers were sequentially bonded together to obtain a multilayer chip with a sealed cavity and covered with carbon fibers. In simulated physiological activities, we used a micro-syringe pump to inject or extract air into the sealed cavity randomly. The carbon fiber layer achieves

random anisotropic contraction and expansion with a maximum height difference of about ± 3 mm from the initial horizontal position.

Animal Tumor Model and Experiment: All procedures were approved by the Southern University of Science and Technology. The mouse tumor model was established using adult BALB/c mice (female; body weight, ~16–20 g). Before inoculation of tumor cells, a depilatory cream was applied to the abdominal area of the mice to remove hair. Subsequently, 1×10^6 4T1 cells dissolved in 50 µL of phosphate buffered saline (PBS) were subcutaneously injected into the anesthetized mice. Upon reaching a tumor volume of 60 mm^3, experimental studies were initiated.

Ex vivo Animal Organ Vessel Angiography Imaging: The experimental animals, New Zealand rabbits (2.5–3 kg), were euthanized in compliance with the regulations formulated by the animal ethics committee at the Southern University of Science and Technology before kidney harvesting. During the organ resecting procedures, retained cannulation using flat-tip needles at the main gateways where organ vessel systems connect to the external environment was performed for each interested vessel system. Then, the organ was treated with decellularization clearing procedures [36]. After the organs achieved tissue optical transparency, the decellularized organs were fixed with a 4% polyoxymethylene solution for at least 24 hours before imaging. We injected the photoacoustic contrast into the renal vein and performed imaging.

Animal Preparation and in vivo Imaging: We used C57BL/6J mice (female; body weight, ~16–20 g) for the *in vivo* brain and tumor imaging, respectively. The animal was initially anesthetized with isoflurane (~2%–4% in 1 L · min^{-1} medical grade air) in an induction chamber via a vaporizer. Then, it was transferred to a heating pad equipped with a nose cone for surgical procedures. During the surgical intervention, anesthesia was sustained at 1.5% in 1 L · min^{-1}. Before any surgical manipulation, the anesthesia status of the animal was confirmed through a toe pinch procedure, whereby the absence of a response indicated an adequate anesthetic depth. The animal was then positioned on a stereotactic frame, with body temperature being maintained by the heating pad. Before surgery, an ophthalmic ointment was applied to the corneal surfaces to avert corneal drying. For mice brain imaging, we gently removed the hair on its head using hair removal cream to avoid the strong photoacoustic signals from the hair. Subsequently, the skin was incised from the middle and the periosteum was removed to expose the mouse brain while keeping the skull intact. A craniotomy was conducted on the mouse to enable the visualization of cortical vessels during imaging. The section of the skull above the area of interest was removed using a dental drill, and the drilling process was interrupted every 30 seconds to prevent overheating. The bone dust was continuously cleared with saline solution. Subsequently, pre-moistened surgical sponges were used to stem any further bleeding from the exposed brain tissue before the animal was moved to the imaging location. For tumor imaging, we gently removed the hair around its tumor region using hair-removing cream. During the imaging, the mice were placed on a heating pad to keep the body temperature at 37°C. Ultrasound gel or saline was applied between the imaging plane and imaging target to ensure ultrasound coupling. The respiration and body temperature were monitored closely to ensure its normal physiological conditions. The animal was euthanized with carbon dioxide after imaging. All animal experiments were carried out in conformity with the protocol approved by Southern University of Science and Technology.

Data and Imaging Processing: All datasets were collected using a customized LabVIEW-based acquisition program. Data processing was performed by customized codes using MATLAB (R2022b). For PAM, to reconstruct the MAP images, we took the amplitude of the photoacoustic A-line signals after Hilbert transform for each pixel. The axial position was determined by quantifying the maximal amplitude position in the A-line signals, assuming a speed of sound of 1500 m · s^{-1} in room-temperature water. A median filter with a window size of 3×3 pixels was applied to the depth image. To obtain the diameter change of each vessel, we constructed the skeleton of the vasculature. We averaged the diameters at different cross sections along the skeleton. In each scanning, we collected 1000 depth-resolved PA signals (A-line) with a step interval of 10 µm in one cross-sectional image (B-scan), and 1000 B-scans with an interval angle of 0.18° to form a volumetric image. Then we carried out MAP of the volumetric image to form a high-resolution PAM image with a pixel number of 1000×1000.

APPENDIX B: SIMULATION OF THE LASER BEAM SPOT SIZE

Figure 5 shows the simulation of the focused laser beam spot size at different locations in the FOV using Zemax.
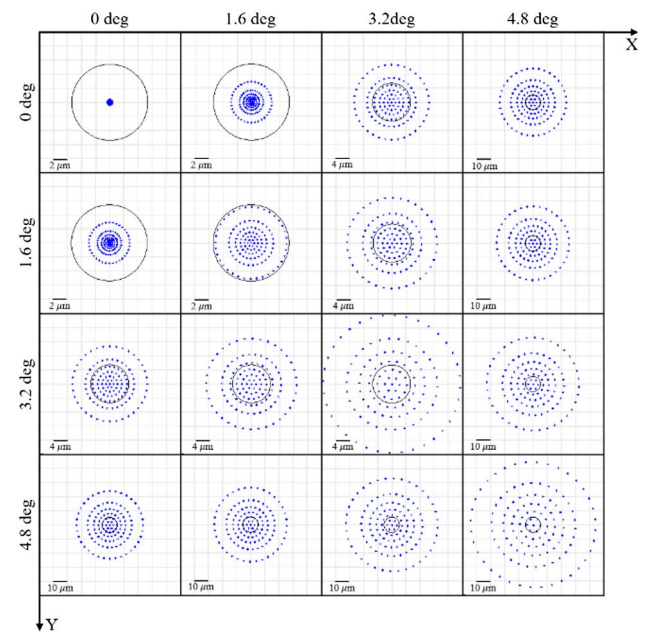

Fig. 5. Simulation of the laser beam spot size per scan point using Zemax.

APPENDIX C: SIMULATION OF THE SYSTEM FOCAL PLANE AND RESOLUTION

Figure 6 shows the process of point-by-point optimization for transforming the optical focal plane to a flat field, which results in achieving uniform resolution throughout the FOV.
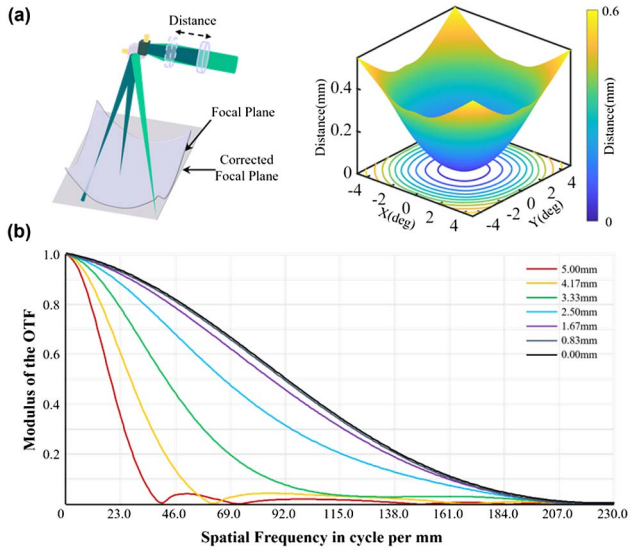

Fig. 6. Simulation of the system focal plane and resolution. (a) The scheme of correcting the focal plane. (b) The average optical transfer function at different sub-FOVs from edge to middle of the whole imaging domain.

APPENDIX D: EXPERIMENTAL DEMONSTRATION OF A LARGE DOF USING HA-PAM

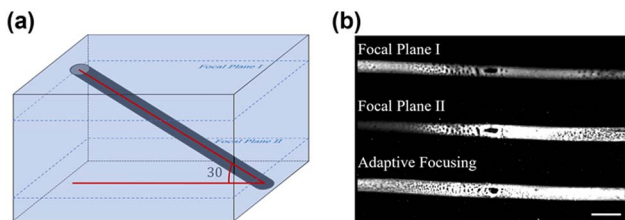Figure 7 shows the imaging results of inclined pencil lead using conventional PAM and HA-PAM.

Fig. 7. Experimental demonstration of a large DOF using HA-PAM. (a) Schematic representation of the inclined pencil lead inserted into an agarose phantom. (b) MAP images of the tilted pencil lead using conventional PAM at different focal planes and HA-PAM, respectively. Scale bar, 1 mm.

APPENDIX E: SCHEMATIC OF THE DYNAMIC OUT-OF-FOCUS PHANTOM EXPERIMENT

Figure 8 shows the construction of the chip chamber. A micro-syringe pump can be used to inject or extract air into the cavity, causing anisotropic expansion and contraction to simulate
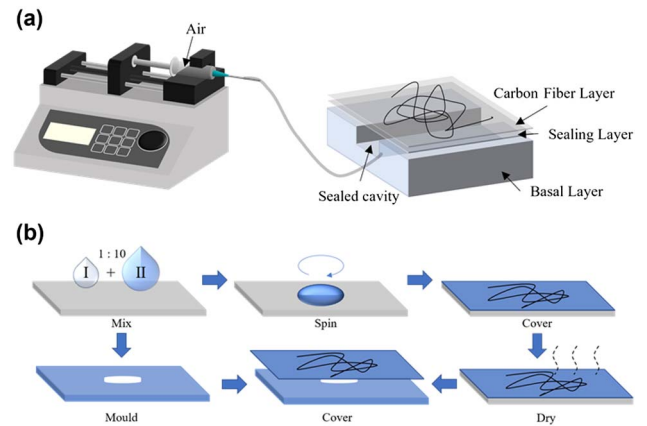

Fig. 8. Schematic of the dynamic out-of-focus phantom experiment. (a) Simulation of dynamic out-of-focus. The contraction and expansion of the carbon fiber layer are achieved by injecting or withdrawing air into the sealed cavity to simulate the physiological activity of brain pulses. (b) Fabrication of the multilayer chip.

physiological phenomena, such as brain pulsation and respiration.

APPENDIX F: CONVENTIONAL PAM IMAGING OF BIOLOGICAL TISSUES WITH LARGE CURVED SURFACES

Figure 9 shows the imaging results of the subcutaneous mouse tumor, the venous system of a resected rabbit kidney, and the mice brain using conventional PAM.
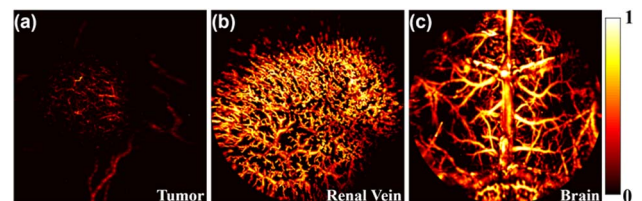

Fig. 9. Conventional PAM imaging of (a) typical mouse subcutaneous tumor, (b) the venous system of a resected rabbit kidney, and (c) a mouse brain.
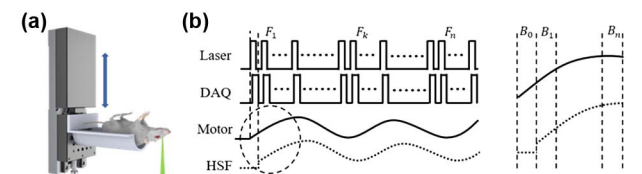

Fig. 10. Schematic of the dynamic out-of-focus in *in vivo* experiment. (a) Simulation of dynamic out-of-focus. The mouse is driven up and down in the direction perpendicular to the imaging surface by a one-dimensional motor to simulate the defocus due to physiological activities. (b) Synchronization sequences of data acquisition and motor movement. During the imaging process, the motor makes random movements. According to the adaptive focusing algorithm, the high-speed focuser (HSF) will follow the corresponding movement of the motor to achieve that the light focus always coincides with the imaging object.

Table 1. Comparison of HA-PAM to Previous PAM Studied on Extending DOF

Methods	Imaging Speed	Resolution	FOV	DOF
HA-PAM (this study)	5 seconds	5.8–6.2 μm	Diameter 10 mm	5 mm
Needle beam [19]	NA	2.3 μm	5.6 × 8 mm	1 mm
Bessel beam [14]	~25 minutes	2.6–4.9 μm	2 × 3 mm	0.483 mm
Bessel beam [16]	~5 minutes	4 μm	4 × 6 mm	0.6 mm
Dynamic focusing [25]	NA	4–8 μm	1.8 × 2.4 mm	0.75 mm
Dynamic focusing [24]	~2 hours	3–5 μm	1.5 × 8 mm	3.2 mm

APPENDIX G: SCHEMATIC OF THE DYNAMIC OUT-OF-FOCUS IN *IN VIVO* EXPERIMENT

Figure 10 shows the schematic of dynamic out-of-focus in *in vivo* experiment using a one-dimensional motor to drive the mouse to move freely in the direction perpendicular to the imaging plane.

APPENDIX H: COMPARISON OF HA-PAM TO PREVIOUS PAM STUDIED ON EXTENDING DOF

Table 1 compares our HA-PAM approach with previously developed methods for extending DOF in PAM.

Author Contributions. L. X. conceived this concept and supervised the overall project design and execution. L. X. and L. L. designed the experiments. L. L. and W. Q. built the imaging system. W. Q., T. L., and J. Z. prepared the sample and animals and performed the imaging experiment. B. L. contributed to the chip preparation. L. L., W. Q., and L. X. drafted the manuscript. All authors provided critical feedback to the manuscript.

Disclosures. The authors declare no conflicts of interest.

Data Availability. The main data supporting the results in this study are available within the paper. The raw datasets are too large to be publicly shared, yet they are available for research purposes upon reasonable request.

REFERENCES

1. J. Fan, J. Suo, J. Wu, H. Xie, Y. Shen, F. Chen, G. Wang, L. Cao, G. Jin, Q. He, T. Li, G. Luan, L. Kong, Z. Zheng, and Q. Dai, "Video-rate imaging of biological dynamics at centimetre scale and micrometre resolution," Nat. Photonics **13**, 809–816 (2019).

2. A. Grinvald, E. Lieke, R. D. Frostig, C. D. Gilbert, and T. N. Wiesel, "Functional architecture of cortex revealed by optical imaging of intrinsic signals," Nature **324**, 361–364 (1986).

3. J. Senarathna, H. Yu, C. Deng, A. L. Zou, J. B. Issa, D. H. Hadjiabadi, S. Gil, Q. Wang, B. M. Tyler, N. V. Thakor, and A. P. Pathak, "A miniature multi-contrast microscope for functional imaging in freely behaving animals," Nat. Commun. **10**, 99 (2019).

4. H. F. Zhang, K. Maslov, G. Stoica, and L. V. Wang, "Functional photoacoustic microscopy for high-resolution and noninvasive in vivo imaging," Nat. Biotechnol. **24**, 848–851 (2006).

5. L. V. Wang and S. Hu, "Photoacoustic tomography: in vivo imaging from organelles to organs," Science **335**, 1458–1462 (2012).

6. L. V. Wang and J. Yao, "A practical guide to photoacoustic tomography in the life sciences," Nat. Methods **13**, 627–638 (2016).

7. W. Qin, Q. Gan, L. Yang, Y. Wang, W. Qi, B. Ke, and L. Xi, "High-resolution in vivo imaging of rhesus cerebral cortex with ultrafast portable photoacoustic microscopy," Neuroimage **238**, 118260 (2021).

8. T. Jin, W. Qi, X. Liang, H. Guo, Q. Liu, and L. Xi, "Photoacoustic imaging of brain functions: wide filed-of-view functional imaging with high spatiotemporal resolution," Laser Photonics Rev. **16**, 2100304 (2022).

9. X. Zhu, Q. Huang, A. DiSpirito, T. Vu, Q. Rong, X. Peng, H. Sheng, X. Shen, Q. Zhou, L. Jiang, U. Hoffmann, and J. Yao, "Real-time whole-brain imaging of hemodynamics and oxygenation at micro-vessel resolution with ultrafast wide-field photoacoustic microscopy," Light Sci. Appl. **11**, 138 (2022).

10. S. Hu, K. Maslov, and L. V. Wang, "Second-generation optical-resolution photoacoustic microscopy with improved sensitivity and speed," Opt. Lett. **36**, 1134–1136 (2011).

11. Y. Yuan, S. Yang, and D. Xing, "Optical-resolution photoacoustic microscopy based on two-dimensional scanning galvanometer," Appl. Phys. Lett. **100**, 023702 (2012).

12. Z. Xu, Y. Pan, N. Chen, S. Zeng, L. Liu, R. Gao, J. Zhang, C. Fang, L. Song, and C. Liu, "Visualizing tumor angiogenesis and boundary with polygon-scanning multiscale photoacoustic microscopy," Photoacoustics **26**, 100342 (2022).

13. J. Shi, L. Wang, C. Noordam, and L. V. Wang, "Bessel-beam Grueneisen relaxation photoacoustic microscopy with extended depth of field," J. Biomed. Opt. **20**, 116002 (2015).

14. B. Jiang, X. Yang, and Q. Luo, "Reflection-mode Bessel-beam photoacoustic microscopy for in vivo imaging of cerebral capillaries," Opt. Express **24**, 20167–20176 (2016).

15. B. Park, H. Lee, S. Jeon, J. Ahn, H. H. Kim, and C. Kim, "Reflection-mode switchable subwavelength Bessel-beam and Gaussian-beam photoacoustic microscopy in vivo," J. Biophotonics **12**, e201800215 (2019).

16. Y. Zhou, N. Sun, and S. Hu, "Deep learning-powered Bessel-beam multiparametric photoacoustic microscopy," IEEE Trans. Med. Imaging **41**, 3544–3551 (2022).

17. J. Yang, L. Gong, X. Xu, P. Hai, Y. Shen, Y. Suzuki, and L. V. Wang, "Motionless volumetric photoacoustic microscopy with spatially invariant resolution," Nat. Commun. **8**, 780 (2017).

18. M. Amjadian, S. M. Mostafavi, J. Chen, Z. Kavehvash, J. Zhu, and L. Wang, "Super-resolution photoacoustic microscopy using structured-illumination," IEEE Trans. Med. Imaging **40**, 2197–2207 (2021).

19. R. Cao, J. Zhao, L. Li, L. Du, Y. Zhang, Y. Luo, L. Jiang, S. Davis, Q. Zhou, A. de la Zerda, and L. V. Wang, "Optical-resolution photoacoustic microscopy with a needle-shaped beam," Nat. Photonics **17**, 89–95 (2023).

20. R. Cao, J. Li, B. Ning, N. Sun, T. Wang, Z. Zuo, and S. Hu, "Functional and oxygen-metabolic photoacoustic microscopy of the awake mouse brain," NeuroImage **150**, 77–87 (2017).

21. C. Yeh, B. Soetikno, S. Hu, K. I. Maslov, and L. V. Wang, "Microvascular quantification based on contour-scanning photoacoustic microscopy," J. Biomed. Opt. **19**, 096011 (2014).

22. B. Li, H. Qin, S. Yang, and D. Xing, "*In vivo* fast variable focus photoacoustic microscopy using an electrically tunable lens," Opt. Express **22**, 20130–20137 (2014).

23. K. Lee, E. Chung, S. Lee, and T. J. Eom, "High-speed dual-layer scanning photoacoustic microscopy using focus tunable lens modulation at resonant frequency," Opt. Express **25**, 26427–26436 (2017).

24. S. Liang, J. Zhou, Z. Guo, D. He, W. Yang, Z. Ye, W. Shao, L. Jing, and S. L. Chen, "Miniature probe for optomechanical focus-adjustable optical-resolution photoacoustic endoscopy," IEEE Trans. Med. Imaging **42**, 2400–2413 (2023).

25. X. Yang, B. Jiang, X. Song, J. Wei, and Q. Luo, "Fast axial-scanning photoacoustic microscopy using tunable acoustic gradient lens," Opt. Express **25**, 7349–7357 (2017).

26. P. Hajireza, A. Forbrich, and R. J. Zemp, "Multifocus optical-resolution photoacoustic microscopy using stimulated Raman scattering and chromatic aberration," Opt. Lett. **38**, 2711–2713 (2013).

27. X. Yang, X. Song, B. Jiang, and Q. Luo, "Multifocus optical-resolution photoacoustic microscope using ultrafast axial scanning of single laser pulse," Opt. Express **25**, 28192–28200 (2017).

28. R. Cao, S. D. Nelson, S. Davis, Y. Liang, Y. Luo, Y. Zhang, B. Crawford, and L. V. Wang, "Label-free intraoperative histology of bone tissue via deep-learning-assisted ultraviolet photoacoustic microscopy," Nat. Biomed. Eng. **7**, 124–134 (2022).

29. Z. Xu, N. Sun, R. Cao, Z. Li, Q. Liu, and S. Hu, "Cortex-wide multiparametric photoacoustic microscopy based on real-time contour scanning," Neurophotonics **6**, 035012 (2019).

30. W. Qi, T. Jin, J. Rong, H. Jiang, and L. Xi, "Inverted multiscale optical resolution photoacoustic microscopy," J. Biophotonics **10**, 1580–1585 (2017).

31. W. Qin, W. Qi, and L. Xi, "Quantitative investigation of vascular response to mesenteric venous thrombosis using large-field-of-view photoacoustic microscopy," J. Biophotonics **12**, e201900198 (2019).

32. J. Zhang, D. Peng, W. Qin, W. Qi, X. Liu, Y. Luo, Q. Guo, and L. Xi, "Organ-PAM: photoacoustic microscopy of whole-organ multiset vessel systems," Laser Photonics Rev. **17**, 2201031 (2023).

33. D. Zhang, R. Li, X. Lou, and J. Luo, "Hessian filter-assisted full diameter at half maximum (FDHM) segmentation and quantification method for optical-resolution photoacoustic microscopy," Biomed. Opt. Express **13**, 4606–4620 (2022).

34. J. Yao, L. Wang, J. M. Yang, K. I. Maslov, T. T. Wong, L. Li, C. H. Huang, J. Zou, and L. V. Wang, "High-speed label-free functional photoacoustic microscopy of mouse brain in action," Nat. Methods **12**, 407–410 (2015).

35. F. Zhong and S. Hu, "Thin-film optical-acoustic combiner enables high-speed wide-field multi-parametric photoacoustic microscopy in reflection mode," Opt. Lett. **48**, 195–198 (2023).

36. Y. Gao, Z. Li, Y. Hong, T. Li, X. Hu, L. Sun, Z. Chen, Z. Chen, Z. Luo, X. Wang, J. Kong, G. Li, H.-L. Wang, H. L. Leo, H. Yu, L. Xi, and Q. Guo, "Decellularized liver as a translucent *ex vivo* model for vascular embolization evaluation," Biomaterials **240**, 119855 (2020).